NONDESTRUCTIVE EVALUATION USING SUPERCONDUCTING QUANTUM INTERFERENCE DEVICE FOR VARIOUS BRAIDED CARBON-FIBER-REINFORCED PLASTIC COMPOSITES UNDER TENSILE LOADING

Y. Hatsukade[1*], Y. Shinyama[1], K. Yoshida[1], T. Kage[1], S. Tanaka[1], Y. Takai[2], M. S. Hassan[3], A. Nakai[3], H. Hamada[3]

[1]*Department of Environmental and Life Sciences, Toyohashi University of Technology, 1-1 Hibarigaoka, Tenpaku-cho, Toyohashi, Aichi 441-8580, Japan.*
[2]*Department of Design, Osaka Sangyo University, 3-1-1 Nakagaito, Daito, Osaka 574-8530, Japan*
[3]*Advanced Fibro-Science Division, Kyoto Institute of Technology, Matsugasaki, Sakyo-ku, Kyoto 606-8585, Japan*

*hatukade@ens.tut.ac.jp

**Keywords:** SQUID, NDE, braided CFRP, tensile test

Abstract
Step-by-step tensile tests were applied to flat-braided carbon-fiber-reinforced plastics with dispersion of carbon nanofibers (CNFs) or insertion of different middle-end carbon-fiber bundles to study their mechanical properties and destructive mechanism. A nondestructive evaluation technique, using a high-temperature superconductor superconducting quantum interference device gradiometer, was also applied to the samples to study their electrical properties and the integrity of the carbon-fiber bundles in the samples. Experimental results indicated that the addition of the CNFs and the insertion of the middle-end bundles attributed to modify not only the mechanical properties, but also the electrical properties of the samples.

1 Introduction

Recently, braided carbon-fiber-reinforced plastic (CFRP) composites, in which carbon-fiber bundles are interlaced in a braided textile (see Figure 1a), have been developed and studied to achieve superior properties compared to conventional woven CFRPs, because of the continuity of the carbon-fiber bundles [1 - 3]. Furthermore, it is expected that the addition of carbon nanofillers in the matrix of the braided CFRPs (Figure 1b) and insertion of the middle-end carbon-fiber bundles in the braided textile (Figure 1c) would improve some CFRP's properties [4, 5]. However, nondestructive evaluation (NDE) technique for the braided CFRPs is yet established, because the fine diameter of the carbon fibers and the complexity of the braided textile require a novel NDE technique having high sensitivity and spatial resolution. Since tensile loading applied to the braided CFRPs is mainly maintained by the continuous carbon-fiber bundles, it is important for the NDE technique to detect ruptures of the carbon-fiber bundles, whose electric conductivity can change significantly when they are broken. Thus, we have proposed a NDE technique using a high-temperature superconductor (HTS) superconducting quantum interference device (SQUID) gradiometer having extremely high sensitivity to electric current and sufficiently high spatial resolution for the braided CFRPs [6]. So far, we demonstrated that the discontinuity of the braided carbon-fiber bundles in tubular-

braided CFRPs could be well detected using the SQUID-NDE technique by visualizing electric current distribution in the CFRP samples while injecting ac currents into the samples. In this study, we prepared various braided CFRP samples based on flat-braided CFRP panels. The samples included carbon nanofibers (CNFs) or the middle-end carbon-fiber bundles. The mechanical properties and destructive mechanism of the samples were studied with observation and measurements of stress-strain curves, while applying step-by-step tensile loading to the samples. The SQUID-NDE technique was tested for evaluating the integrity of the carbon-fiber bundles in the samples, before, during, and after the tensile loading.
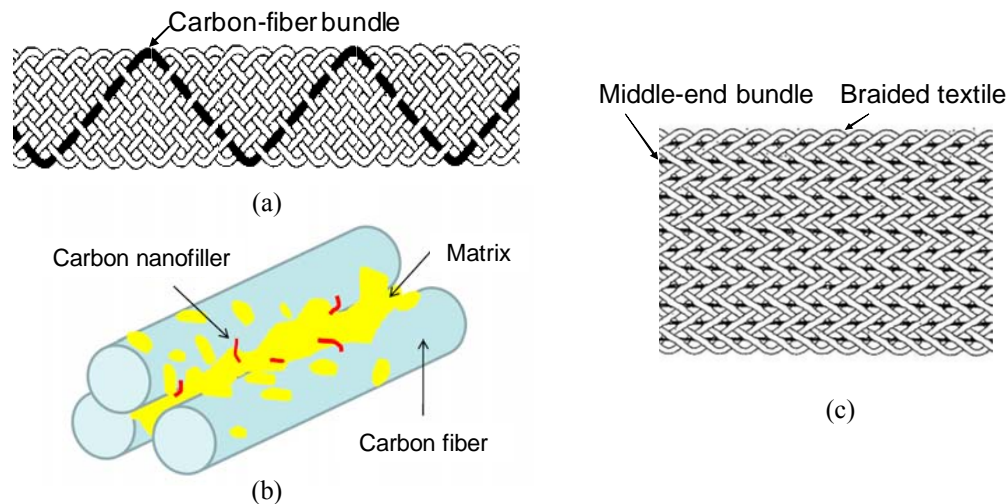
Figure 1. Schematic illustrations of braided CFRPs. (a) Braided textile with continuous carbon-fiber bundles. In actual samples, neighboring bundles are touching with each other. (b) Dispersion of carbon nanofillers in matrix and carbon fibers. (c) Inserted middle-end bundles in braided textile.

2 Samples and step-by-step tensile tests

2.1 Flat-braided CFRP samples

For this study, we fabricated ±45° flat-braided CFRP panels, with and without CNFs. These panels contain 25 carbon-fiber bundles (HTS40, Toho Tenax) braided together at angles of ±45° into flat textiles, and epoxy resin (JER828, Japan Epoxy Resins Co. Ltd.). Each carbon-fiber bundle was composed of 12000 carbon fibers with the average diameter and specific electrical resistivity of 7 μm and 1.6×10^{-3} Ω·cm. The average tensile strength, tensile modulus, and elongation of the bundles were 4200 MPa, 240 GPa, and 1.8 %, respectively. Vapor grown CNFs (VGCF, Showa Denko K.K.) were dispersed throughout one panel, which was labeled as 45HTS-NF. The average diameter, length, and specific resistivity of the CNFs were about 150 nm, 10 μm, and 10^{-4} Ω·cm, respectively. The dimensions of the sample 45HTS-NF were 151 mm × 41 mm × 1.0 mm. From observation of a sample of the same kind as 45HTS-NF, using scanning electron microscopy, it was demonstrated that the CNFs were distributed not only in the epoxy resin matrix, but also in between the carbon-fiber bundles as schematically shown in Figure 1b [5]. For comparison, the CFRP panel without the CNFs was prepared and labeled as 45HTS. The dimensions of 45HTS were almost same as 45HTS-NF.

Three ±25° flat-braided CFRP panels, with different middle-end carbon-fiber bundles were also fabricated. These CFRP panels contained 25 carbon-fiber bundles (UTS50, Toho Tenax) braided at angles of ±25° into flat textiles, and the same epoxy resin as 45HTS. The carbon-fiber bundle UTS50 was composed of 12000 carbon fibers with the average diameter and specific electrical resistivity of 6.9 μm and 1.6×10^{-3} Ω·cm. The tensile strength, tensile modulus, and elongation of the bundles were 4900 MPa, 240 GPa, and 2%, respectively. In these panels, three different middle-end carbon-fiber bundles were inserted: ten UTS50 bundles, ten XN05 (Nippon Graphite Fiber Corp.) bundles, and ten XN60 (Nippon Graphite

Fiber Corp.) bundles, respectively. The parameters of the used carbon-fiber bundles were summarized in Table 1. These three panels were labeled as 25UT-UT50, 25UT-XN05, and 25UT-XN60, respectively. We note that the electric resistivity of XN05 is highest (2.8×10^{-3} $\Omega \cdot$cm), while that of XN60 is lowest (0.7×10^{-3} $\Omega \cdot$cm). The dimensions of the samples 25UT-UT50, 25UT-XN05, and 25UT-XN60, were 250 mm × 28 mm × 1.5-1.7 mm.

Grade	Filament count	Tensile strength [MPa]	Tensile modulus [GPa]	Elongation [%]	Filament diameter [μm]	Electrical resistivity [Ω·cm]
HTS40	12000	4200	240	1.8	7	1.6×10^{-3}
UTS50	12000	4900	240	2	6.9	1.6×10^{-3}
XN05	6000	1100	54	2	10	2.8×10^{-3}
XN60	6000	3430	620	0.6	10	0.7×10^{-3}

Table 1. Properties of carbon-fiber bundles used for flat-braided textiles (HTS40 and UTS50) and middle-end bundles (UTS50, XN05, and XN60).

2.2 Step-by-step tensile tests

The CFRP samples were tested by step-by-step tensile loading to clarify their mechanical properties and destructive mechanisms. Tensile loading was applied to each sample in the longitudinal direction at a crosshead speed of 1 mm/min., while one surface of each sample was monitored and the stress-strain curve was measured using strain gauges. The surfaces of the samples were painted at times with white watercolor to observe surface defects. Once the initial tensile loading was applied to each sample, the loading was increased gradually. When an obvious decrease in mechanical strength was occurred, or when any defect was identified, the loading was stopped, and then released to apply below-described SQUID-NDE technique to the sample, in order to evaluate the integrity of their carbon-fiber bundles and electrical properties. We note that the stress-strain curves of the most samples did not return to the starting point after release of the loading. Therefore, after the application of the SQUID-NDE technique, we applied loading to the samples again until the measured strain reached to the maximum value at the previous loading, and thereafter, incremental quantities of strain and stress were measured, and then added to the initial stress-strain curves, for simplicity of plotting. By this process, a continuous stress-strain curve was obtained for each sample.

Figure 2 shows the stress-strain curves of the samples 45HTS-NF and 45HTS, with photographs of sample surfaces at certain damage stages. In the case of 45HTS-NF, the stress increased nonlinearly with increasing strain from the virgin stage, indicated by "a". When the stress and strain reached 340 MPa and 0.055, cracks occurred on the right side of the sample (indicated by the dotted oval), although no corresponding decrease in stress was measured ("b"). This means that the cracks were only matrix cracks on the matrix-rich side, and not accompanied by carbon-fiber fracture or delamination. Just before the strain reached about 0.06, the final fracture suddenly occurred at the maximum measured stress of 350 MPa ("c").

In the case of 45HTS, the stress also increased nonlinearly with the strain, similarly to 45HTS-NF, from the virgin stage ("d"). When the strain reached 0.056, at the maximum stress of 275 MPa, the stress dropped with the occurrence of a crack in the right-lower area with an angle of about 30° ("e"). After this first drop in stress, slight increases and drops repeated with propagation of new zigzag cracks along the first crack. This repeated increase and drop indicated that delamination between the carbon-fiber bundles and relocation of the bundles, occurred in turn. The final fracture occurred with the carbon-fiber fracture when the strain reached over 0.072 ("f"). The results demonstrated that the addition of CNFs could give greater mechanical tensile strength to the braided CFRP, although the measured maximum strain was smaller than that of the braided CFRP without CNFs.
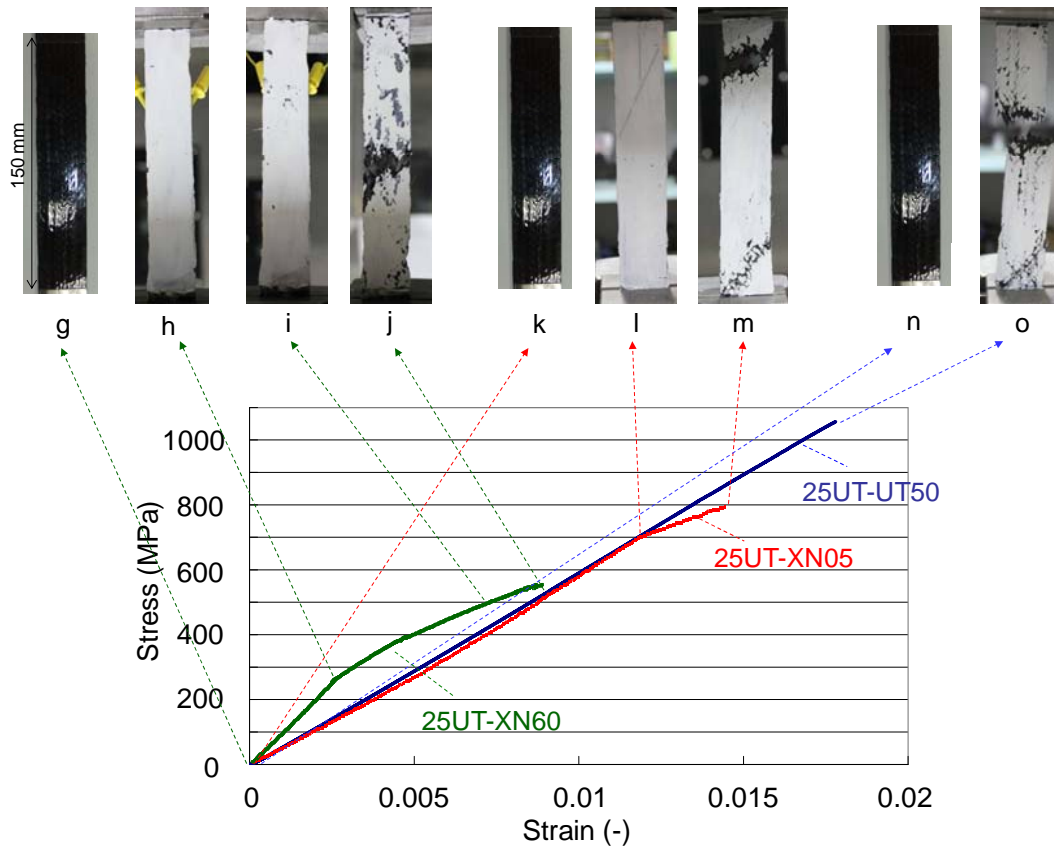
Figure 3 shows the stress-strain curves of the samples 25UT-UT50, 25UT-XN05, and 25UT-XN60, with photographs of sample surfaces at certain damage stages. In the case of 25UT-UT50, the stress increased linearly with the strain, with the initial tensile modulus of about 59 GPa. When the stress and strain reached 1055 MPa and 0.0178, the final fracture suddenly occurred near the center of the sample ("o"). We note that any cracks did not occur until the final fracture. It was interesting that slanting zigzag cracks at an angle of about 45° was observed on the lower part of the sample. These cracks were thought to be caused by reaction of the final fracture. Vertical zigzag cracks were observed along some middle-end bundles.

In the case of 25UT-XN05, the stress increased almost linearly with the strain, with the initial tensile modulus of about 58 GPa, similarly to 25UT-UT50. When the stress and strain reached 700 MPa and 0.012, small horizontal cracks occurred ("l"). After the occurrence of the cracks, the tensile modulus slightly decreased, and when the stress and strain reached 800 MPa and 0.0145, the final fracture occurred in the upper part, concomitantly with occurrence of slanting zigzag cracks at an angle of about 45° in the bottom part, similarly to 25UT-UT50 ("m"). However, vertical zigzag cracks, which occurred in 25UT-UT50, were not observed.

In the case of 25UT-XN60, the stress increased linearly with the strain, with the higher initial tensile modulus of about 104 GPa, than those of 25UT-UT50 and 25UT-XN05. When the stress and strain reached 255 MPa and 0.0025, small horizontal cracks occurred ("h"). After the occurrence of the cracks, the tensile modulus slightly decreased. Occurrence of new cracks and slight decrease in the modulus repeated a few times such as indicated by "i", and when the stress and strain reached 550 MPa and 0.009, the final fracture occurred in the center part of the sample ("j"). Slanting zigzag cracks at an angle of about 25° occurred in both the top and bottom parts. Vertical zigzag cracks, which occurred in 25UT-UT50, were not observed, but peeling-off of the watercolor paint was observed in relatively wide parts on 25UT-XN60.

From those results, it was shown that 25UT-UT50, in which the same carbon-fiber bundles were used in the textile and middle-end bundle, had the greatest destructive strength and strain among the samples. 25UT-XN05, in which XN05 with much smaller tensile modulus and the same elongation was used as the middle-end bundles, had the same initial tensile modulus, although the destructive strength and strain were smaller than those of 25UT-UT50. This should be because of the 4 times smaller tensile strength of the XN05 than that of UTS50.
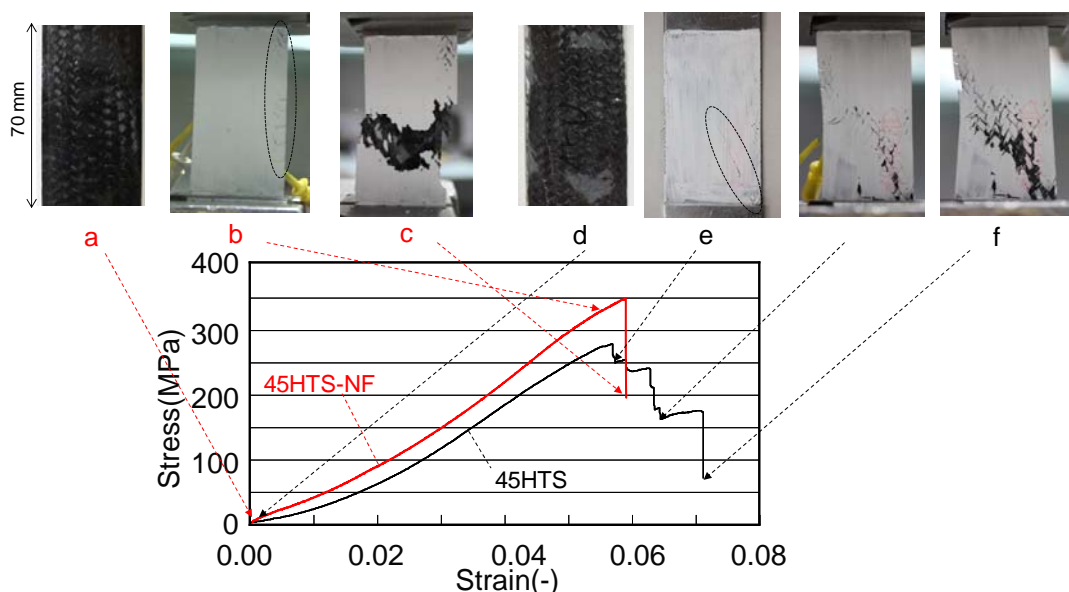
Figure 2. Stress-strain curves of the samples 45HTS-NF and 45HTS. Photographs of the samples at certain damage stages are shown together. Some cracks are emphasized with the dotted ovals. The photographs at "a" and "d" were taken before they were painted by watercolor.

25UT-XN60, in which XN60 with higher tensile modulus and smaller elongation was used as the middle-end bundles, had the highest initial tensile modulus among the samples. The destructive strength and strain of 25UT-XN60 were smallest probably because of the smallest elongation of XN60.

Figure 3. Stress-strain curves of the samples 25UT-UT50, 25UT-XN05, and 25UT-NX60. Photographs of the samples at certain damage stages are shown together. The photographs at respective virgin stages were taken before they were painted by watercolor.

3 SQUID-NDE

3.1 SQUID-NDE technique

At the certain damage stages before, during, and after the tensile loading, ex-situ SQUID-NDE technique was applied to the samples, using a HTS-SQUID gradiometer with current injection. A planar first-order HTS-SQUID gradiometer, with small differential pickup coil and a small baseline, functions as a current detector with high spatial resolution when a liftoff between the gradiometer and a conductive panel sample is short enough such that the liftoff is comparable to the baseline, as described elsewhere [7]. In this study, we put electrical terminals on both ends of each sample to induce an ac current in the longitudinal direction, while applying an ac voltage across each sample. In such case, distribution of the resultant flowing current in the sample depended on distribution of electrical resistivity in the sample. The distribution of the electrical resistivity was determined by the geometry of the braided textile, and contacting resistivity between the bundles in the braided CFRPs. The CNFs existing in between the bundles, and the middle-end carbon-fiber bundles interlaced in the braided textile would also attribute to the current distribution. When such a sample, in which an ac current is being induced, is set on the *x-y* plane, the induced current densities J_x and J_y in the sample have similar distributions as the magnetic field gradients dB_z/dy and $-dB_z/dx$ in an *x-y* plane near the sample. These relationships $\mu_0 J_x \approx dB_z/dy$, and $\mu_0 J_y \approx -dB_z/dx$, between the currents and the field gradients, can be derived from the Maxwell's equation, $\nabla \times \mathbf{H} = \mathbf{J}$ [7].

Based on this principle, we employed a SQUID-NDE system using a small HTS-SQUID gradiometer and an automated *xy* stage, which was described elsewhere [6]. In this study, we set each sample on the *xy*-stage, and induced an ac current of 7 mA at 800 Hz in the longitudinal directions in the cases of 45HTS-NF and 45HTS. In the cases of 25UT-UT50, 25UT-XN05, and 25UT-XN60, the induced currents were 2.6 mA, 4.2 mA, and 10.8 mA at 800 Hz, respectively, which depended on the electrical resistivity of each sample. The distributions of the field gradients dB_z/dy and dB_z/dx above each sample were scanned with a liftoff of 2–3 mm, while changing the direction of the gradiometer to measure dB_z/dy at first, and then dB_z/dx next. The scanning intervals in the *x* and *y* directions were 1 mm. The measured area above the samples was the area shown in the photographs in Figures 2 and 3. We converted the field gradient distributions of dB_z/dy and -dB_z/dx into the distributions of current components J_x and J_y based on the field gradient to current conversion scheme [7]. In this paper, the scale of the converted current distributions was the voltage of the SQUID output, which was proportional to the field gradients dB_z/dy and -dB_z/dx.
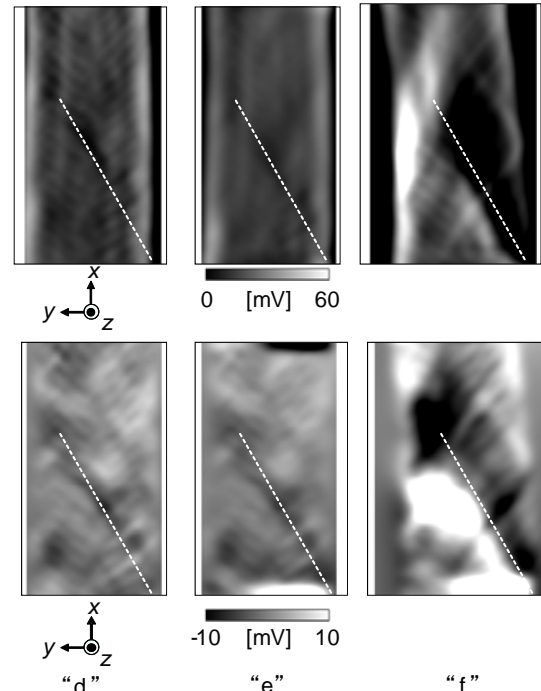
3.2 Measurement results of 45HTS-NF and 45HTS

Figures 4 and 5 show the measurement results of the converted J_x and J_y distributions in 45HTS-NF and 45HTS. The left-upper and left-lower current maps in Figure 4 show the J_x and J_y distributions at the virgin stage "a" with a liftoff of 2 mm. In the current map of J_x, two peaks were measured along both sides, whereas the current was weaker in the middle area of the sample. Conversely, a stripe pattern along the braided bundles was clearly visible in the current map of J_y. The same stripe pattern can be hardly seen in the J_x map because the peaks along the sides were dominant. From the stripe patterns, it could be seen that the currents flowed mainly along the ±45° bundles continuously. The patterns of the same kind were also observed in the case of 45HTS at the virgin stage "d", as shown in Figure 5. However, the peak along the edges observed in 45HTS was weaker and narrower, and the stripe pattern was less uniform than those of 45HTS-NF. It is inferred that these differences were attributed to the addition of CNFs in 45HTS-NF, because it is thought that CNFs in between the bundles should decrease the contacting electrical resistivity between the bundles, thereby averaging (or smoothing) the current density among the bundles and increasing the J_x component, which should flow in the *x* direction through neighboring bundles owing to the assistance of the CNFs [4]. The current distributions shown in the middle-upper and middle-lower maps of Figure 4 (at "b") did not quite differ from those at "a", with the exception of less spatial resolution owing to the longer liftoff of 3 mm. In the tensile test, 45HTS-NF broke suddenly, and most of the bundles were fractured. This damage mechanism was quite different from that of 45HTS and was likely due to the presence of the CNFs, which increased the maximum stress of the sample, as shown in Figure 2. Because of the CNFs, not only the strength of the matrix, but also the strength of the mechanical connection between the bundles should be increased. Thus, delamination between the bundles and relocation of the bundles, which occurred in 45HTS, did not occur in 45HTS-NF. This led to the firm transmission of stress between neighboring bundles fixed with the strengthened matrix, resulting in the sudden final fracture. At the final stage "c", only several bundles were not broken in 45HTS-NF, as shown in the right-upper and right-lower maps of Figure 4, because several strong current appeared.

In the case of 45HTS, it appears that the first crack did not cause a clear change in the current distribution, as shown in the middle-upper and middle-lower maps of Figure 5 ("e"). As mentioned, it was estimated that the crack, which caused the drop in stress, should cause the delamination and relocation of the bundles. However, because the mechanical and electrical connections between the neighboring bundles in 45HTS should be weaker than those of 45HTS-NF, the delamination and relocation did not seriously affect to the current distribution. After the final fracture, it was estimated that most bundles in the right-side area of the first

crack line, which is indicated by the dotted line in Figure 5, were broken, whereas those in the left-side area of the line were almost not damaged, from observation of the current distribution. We note that there was a low current density area on the first crack line even at the virgin stage "d", which is indicated by the dotted line. This may indicate a possibility to predict the location of the final fracture by this NDE technique.
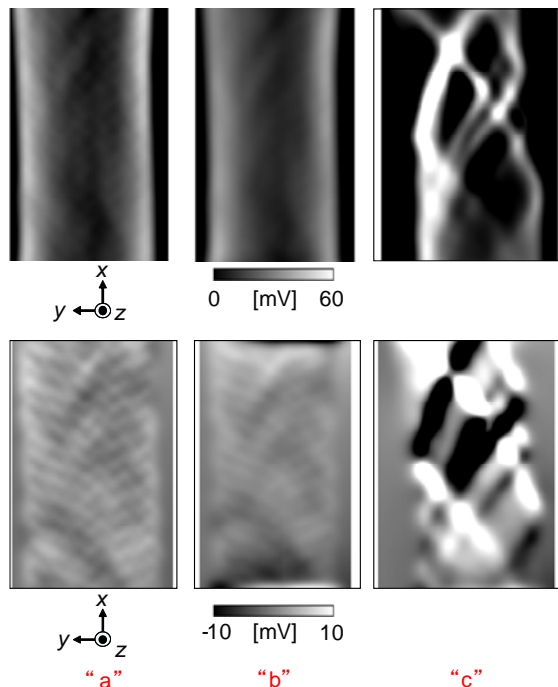
Figure 4 Measured J_x (upper) and J_y (lower) maps of 45HTS-NF at damage stages "a", "b", and "c".

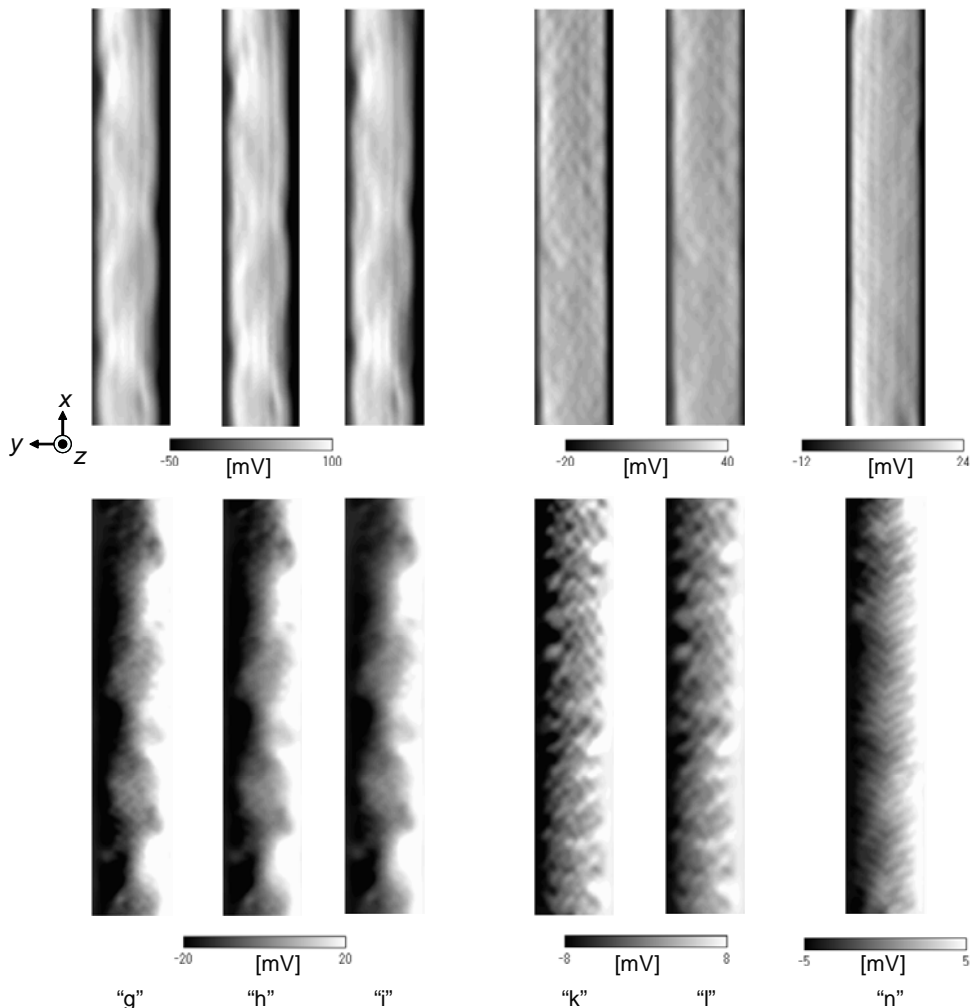**Figure 5** Measured J_x (upper) and J_y (lower) maps of 45HTS at damage stages "d", "e", and "f".

3.3 Measurements and results of 25UT-UT50, 25UT-XN05, and 25UT-XN60

Figure 6 shows the measurement results of the converted J_x and J_y distributions in 25UT-UT50 at damage stage "n" in Figure 3, 25UT-XN05 at "k" and "l", and 25UT-XN60 at "g", "h", and "i", respectively. The scales in Figure 6 were normalized according to the currents flowing in the respective samples. At the respective virgin stages ("g", "k", and "n"), the current distributions were quite different. In 25UT-XN60 with the middle-end bundles of the lowest resistivity, the current in the x direction was dominant compared to the other results, while the current in the y direction, which appeared along the braided textile, was weakest among the samples. These results indicate that the induced current flowed mainly in the ten XN60 middle-end bundles, and partially in the braided textile made of UTS50. The current in the x direction in 25UT-UT50 was more dominant that that in 25UT-XN05. These results well agreed with the fact that the resistivity of UTS50 was lower than that of XN05. In this study, it was shown that the observed cracks before the final fractures, which occurred in 25UT-XN60 at "h" and "i", and in 25UT-XN05 at "l", attributed to reduce the sample's tensile moduli, but not to change the current distributions significantly as shown in Figure 6. These results indicate that these cracks were likely due to rupture of small number of carbon fibers in the middle-end bundles in the respective samples, and consequent debonding between the damaged middle-end bundles and the braided textile. We thought that the energy of the debonding was transmitted to the surface, resulting in the observed surface cracks.

4 Summary

The experimental results obtained by the destructive tests and nondestructive evaluation, indicated that the addition of the CNFs and the insertion of the different middle-end bundles

attributed to modify not only the mechanical properties, but also the electrical properties of the samples. The damage analysis on the bundles at the final stages of the samples with the middle-end bundles is being studied.

Figure 6 Measured J_x (upper) and J_y (lower) maps of 25UT-XN60 at "g", "h", and "i", 25UT-XN05 at "k", and "l", and 25UT-UT50 at "n".

References

[1] Chou T.-W., Ko F.K. Textile Structural Composites. in *Composite Materials Series Vol. 3*, Elsevier Science Publishers BV, Amsterdam, pp. 1-26 (1989).

[2] Falzon P.J., Herszberg I. Mechanical performance of 2-D braided carbon/epoxy composites. *Composites Science and Technology*, **58**, pp. 253-265 (1998).

[3] Nakai A., Ohki T., Takeda N. Hamada H. Mechanical properties and micro-fracture behavior of flat braided composites with a circular hole. *Composite Structures*, **52**, pp. 315-322 (2001).

[4] Gojny F.H., Wichmann M.H.G., Fiedler B., Kinloch I.A., Bauhofer W., Windle A.H., Schulte K. Evaluation and identification of electrical and thermal conduction mechanisms in carbon nanotube/epoxy composites, *Polymer*, **47**, pp.2036-2045 (2006).

[5] Takai Y. Design for advanced carbon fiber braided composites. Ph. D. thesis, Kyoto Institute of Technology, Kyoto (2011).

[6] Shinyama Y., Hatsukade Y., Takai Y., Aly-Hassan M.S., Nakai A., Hamada H. Nondestructive evaluation of braided carbon fiber composites with artificial detect using HTS-SQUID gradiometer. *Physica C*, **471**, pp. 1242-1245 (2011).

[7] Hatsukade Y., Aly-Hassan M.S., Kasai N., Takashima H., Hatta H., Ishiyama A. SQUID-NDE method on damaged area and damage amount of detects in composite materials. *IEEE Transactions on Applied Superconductivity*, **13**, pp. 207-210 (2003).